

RSC Advances



This is an *Accepted Manuscript*, which has been through the Royal Society of Chemistry peer review process and has been accepted for publication.

Accepted Manuscripts are published online shortly after acceptance, before technical editing, formatting and proof reading. Using this free service, authors can make their results available to the community, in citable form, before we publish the edited article. This *Accepted Manuscript* will be replaced by the edited, formatted and paginated article as soon as this is available.

You can find more information about *Accepted Manuscripts* in the [Information for Authors](#).

Please note that technical editing may introduce minor changes to the text and/or graphics, which may alter content. The journal's standard [Terms & Conditions](#) and the [Ethical guidelines](#) still apply. In no event shall the Royal Society of Chemistry be held responsible for any errors or omissions in this *Accepted Manuscript* or any consequences arising from the use of any information it contains.

Evolution of structural and thermal properties of carbon-coated TaC nanopowder synthesized by single step reduction of Ta-Ethoxide

Loveleen K. Brar, Gourav Singla, O. P. Pandey*

School of Physics and Materials Science, Thapar University, Patiala (India)

*Corresponding author:-

Dr. O.P. Pandey

Senior Professor

School of Physics and Materials Science, Thapar University, Patiala (India)

Tel.: +91 175 2393130; fax: +91 175 2393020, E-mail address:- oppandey@thapar.edu

Ms. Loveleen Kaur Brar (First Author)

Assistant Prof.

School of Physics and Materials Science, Thapar University, Patiala (India)

E-mail address: brarloveleen@thapar.edu

Mr. Gourav Singla (Co-Author)

Graduate Student,

School of Physics and Materials Science, Thapar University, Patiala (India)

E-mail address: gsinghla@gmail.com

Evolution of Structural and Thermal Properties of Carbon-Coated TaC Nanopowder Synthesized by Single Step Reduction of Ta-Ethoxide

ABSTRACT

Carbon-coated nano Tantalum Carbide (TaC) has been synthesized at 800 °C using Tantalum-Ethoxide precursor by the single step chemical reaction route without using any external carbon source. The XRD results of the synthesized samples indicate that formation of TaC starts immediately upon heating but the complete transformation is observed only after 10 hrs of holding at 800 °C. The 10 hrs sample shows distinct decarburization and oxidation peaks in DSC/DTG. The surface weighted sizes obtained from double-Voigt method were confirmed by BET. The BET analysis shows that synthesized powders have large surface area and contain a mixture of micropores and mesopores. The morphology and particle size distribution analysis shows that the powders are of faceted to spherical shape with thin carbon coating having size variation primarily between 20-40 nm. DSC/TG, XRD and microstructure analysis results have been used to predict the mechanism for the formation of the carbon coated nano-TaC particles.

Keywords: Nanoparticles; Tantalum Carbide; Chemical reaction method; double-Voigt integral breadth method; carbon coated.

1. Introduction

Group IV-VI transition metal carbides have high potential for industrial applications. As a result of a unique combination of metal-nonmetal bonding and metal-metal bonding Tantalum Carbide (TaC) exhibits a combination of outstanding properties such as extreme hardness, high melting point, high electronic conductivity, high oxidation resistance as well as resistance to chemical attack and thermal shock.¹⁻⁷ Moreover, the catalytic activity of TaC further widens the scope for its industrial applications. Application of TaC as a catalyst and catalyst support material for ammonia decomposition, hydrodenitrogenation and hydrogen dissociation reactions has opened a new area of development of nano TaC particles having high surface area.^{3,4,8-12} Apart from these, the superior mechanical properties of the nano-sized powders have further increased the demand for nano-TaC.¹³ Hence, synthesis of pure phase nano-TaC with large specific surface area is of paramount importance for catalytic as well as for the traditional applications. Conventional synthesis methods of TaC powder are energy intensive and require careful monitoring. Moreover, these also result in coarsening of grains.^{3,14,15}

Over last few years many methods have emerged for the synthesis of TaC nano-particles. Ta₂O₅ and TaCl₅ have emerged as the most common precursors for the synthesis of TaC. These along with various carburization sources have been used for the synthesis of nano-TaC either in vacuum or inert atmosphere where the single phase TaC nano-particles are obtained only at temperatures greater than 1000 °C.^{4,14-21} Addition of catalysts such as Mg, Ni^{7,16} and/or halogenation agents such as NaF^{16,20} can reduce the reduction temperature. Recent reports indicate that TaC can be synthesized using TaCl₅ precursor at temperature range of 600 - 900 °C.^{5,6,22} Use of organic precursors has mostly been limited to multistep processes involving formation of dispersed Ta₂O₅ followed by carburization using an external carbon source.^{16,23,24}

Cubic carbides like TaC can tolerate large deficiencies of carbon without changing the structure type.^{1,22,25} But the carbon content is related with the mechanical properties of the material and also the surface stoichiometric properties which ultimately affect the catalytic response of the material.^{1,4} So the synthesized TaC powders need to be characterized for size, specific surface area as well as stoichiometry.²² The final characteristics of the synthesized product depends largely on the carbon content in the reaction mixture as well as the homogeneity of mixing.²⁶ In most of the currently prevalent methods the reduction in reaction temperature and product size is achieved by multiple steps involving formation of nano – Ta₂O₅ followed by its mixing with carbon source and/or heating in reducing carbon rich atmosphere. Slight variation in any one of the steps can change the properties of the final product drastically.^{22,26,15}

To control the particle size and maintain the purity of the synthesized transition metal carbide nano powder, the single step chemical reaction method in autoclave has been developed.^{27,28} In the present study we report the single step synthesis of carbon-coated nano-TaC. Commercial grade Ta-Ethoxide has been used as Ta precursor as well as carbon source. Here the *in situ* carbon, produced during the decomposition of Ta-Ethoxide, has been utilized for the reduction and carburization in the presence of reducing agent Mg at 800⁰C to get TaC nanopowder. To the best of our knowledge synthesis of nano TaC from Ta-Ethoxide or any other organic precursor has not been reported so far at such a low temperature.

2. Experimental Section

2.1 Synthesis of TaC nanocrystals.

For the synthesis of TaC nano powder, Ta-Ethoxide (Ta-E, Ta₂(C₂H₅O)₅, 99.99%, Sigma Aldrich) and Mg (99%, Loba Chemie) in molar ratios of 1:7 were sealed in a stainless steel

autoclave of 20 ml capacity. The entire assembly was placed inside the furnace. The temperature of the furnace was raised from room temperature to 800 °C slowly (5⁰/min) and autoclave was finally maintained at the extreme temperature for different durations (2, 5, 8, 10 and 12 hrs). The autoclave was then allowed to cool to room temperature. The resultant product was collected and leached with diluted HCl (1:1) to remove magnesium oxide (MgO) and unreacted Mg. After leaching, the powder was washed several times with double distilled water to remove any traces of unreacted acid. Finally, the powder was washed with acetone and dried in vacuum at 100 °C.

2.2 Characterization.

The X-ray diffraction (XRD) study of the synthesized products was done to identify and structurally characterize the crystalline phases present. The XRD of the samples was performed using PANalytical X-Pert-Pro with CuK α radiation ($\lambda = 1.5406 \text{ \AA}$) obtained from the copper target using an inbuilt Ni filter. The X-ray powder diffraction data were collected for all samples at room temperature between $20^\circ \leq 2\theta \leq 80^\circ$ with a step size of 0.0130° (2θ). Phase identification from the ICDD data base (using X-Pert High Score Plus) was further confirmed by Rietveld refinement of all the XRD patterns (using FullProf Suite).

X-ray line profile analysis allows for meaningful determination of size and strain of the product which can be used to correlate the microstructure of the synthesized powders with their properties. Scherrer relation is still the most commonly used method for the determination of domain size for coherent scattering in the given sample. The domain size obtained from the Scherrer relation is a volume weighted quantity. Scherrer relation uses full width at half maxima (FWHM) of the XRD peaks for the determination of domain size, t :

$$t = \frac{K\lambda}{FWHM \cos\theta} \quad (1)$$

Where, K: Shape factor, θ : Bragg angle, λ : X-ray wavelength

Wilson defined “integral breadth apparent size” where the integral breadth, β (A/I_0 , A: Area of the peak, I_0 : Maximum Intensity) is used instead of FWHM²⁹ to define the volume weighted crystallite size, $\langle D_V \rangle$:

$$\langle D_V \rangle = \frac{K\lambda}{\beta \cos\theta} \quad (2)$$

For both the above cases the peak broadening is attributed to the coherently diffracting domain size. Stokes and Wilson gave the relation for broadening solely due to strain.²⁹ The maximum strain, e , is given by:

$$\beta = 4 e \tan\theta \quad (3)$$

Williamson-Hall plot is used extensively to separate the size and strain effects:^{29,30}

$$\beta \cos\theta = \frac{K\lambda}{\langle D_V \rangle} + e 4\sin\theta \quad (4)$$

In the above equation it is assumed that the strain and size broadening functions are Lorentzian in nature. Since Lorentzian or Gaussian functions cannot satisfactorily model the specimen broadening exclusively, it is assumed that both size and strain effects are approximated by either Voigt or its approximation - pseudo-Voigt function.³¹ In the present case individual peaks have been fitted with pseudo-Voigt function which is a linear combination of Lorentzian ($L(x)$) and Gaussian ($G(x)$) functions.^{31,32}

$$F(x) = \eta L(x) + (1-\eta) G(x) \quad (5)$$

Where, η : mixing parameter

For the peak fitting the peak shape is assumed to be symmetrical. The split pseudo-Voigt function is known to provide better fits. Here, the results after best-fit were chosen taking into account the minimum error as well as realistic values for the fitting parameters. The obtained integral breadths are a combination of instrumental and specimen broadening so the instrumental corrected integral breadths were estimated from the measured data.³¹

Single line analysis: De Keijser et al.,²⁹ in the case of a single line analysis, assumed that the Lorentz component of the line profile is solely due to the crystallite size and that the Gaussian contribution arises from the strain. Hence the apparent domain size for a hkl reflection can be deduced using the relation (2) replacing β by β_L and the strain is obtained using the relation (3) replacing β by β_G , β_L and β_G being the Lorentzian and Gaussian parts of the integral breadth. For the case of a Gaussian micro-strain distribution it is possible to calculate the local root-mean-square strain:³¹

$$\langle \epsilon^2 \rangle^{1/2} = \sqrt{\frac{2}{\pi}} e \quad (6)$$

Voigt multiple-line integral-breadth methods: The Lorentzian and Gaussian components of the size and strain integral breadths follow the convolution principle and the various components can be separated. Warren definition of mean-square strain requires that the Lorentz and Gauss distortion integral breadths depend differently on s ($= \frac{2 \sin \theta}{\lambda}$) and the multiple-line Voigt method by Langford becomes:^{29,32}

$$\beta_L = (\beta_{SL} + \beta_{DL} \frac{s^2}{s_0^2}) \quad (7)$$

$$\beta_G^2 = \left(\beta_{SG}^2 + \beta_{DG}^2 \frac{s^2}{s_0^2} \right) \quad (8)$$

Where,

β_{SL} , β_{DL} are modified Lorentzian components of size and strain integral breadth.

β_{SG} , β_{DG} are modified Gaussian components of size and strain integral breadth.

and,
$$\text{Modified } \beta = \frac{\beta(2\theta) \cos\theta}{\lambda} \quad (9)$$

This method is called “Double-Voigt” method. β_L and β_G^2 are plotted *w.r.t.* s^2 and the corresponding strain and size components β_{SL} , $\beta_{DL}(hkl)$, β_{SG} , $\beta_{DG}(hkl)$ are obtained. The analytical expressions for the volume weighted domain size, $\langle D_v \rangle$, strain, $\langle \varepsilon^2 \rangle^{1/2}$ and size coefficients, $A_s(L)$ are:^{29,31}

$$\langle D_v \rangle = \left[\frac{\beta_{SL} + (\beta_{SL}^2 + \beta_{SG}^2)^{1/2}}{2} \right]^{-1} \quad (10)$$

$$\langle \varepsilon^2(L) \rangle = \frac{1}{s^2} \left[\frac{\beta_{DG}^2}{2\pi} + \frac{\beta_{DL}}{\pi^2} \frac{1}{L} \right] \quad (11)$$

$$A_s(L) = \exp(-2L\beta_{SL} - \pi L^2 \beta_{SG}^2) \quad (12)$$

Equation (11) is used to determine the r.m.s. strain distribution *w.r.t.* size (L) and direction. The initial slope of the $A_s(L)$ vs L graph is used to determine the surface weighted domain size.^{29,31}

Surface weighted domain size determination of the powder is important for the applications where the active surface area is important e.g. catalysis.³³ The single line and double line analysis were carried out using Origin software.

DTA/TG (Diamond TG/DTA, Perkin Elmer) and DSC/TG (NETZSCH STA 449F3) were done at a heating rate of 5 °C/min in air atmosphere to determine the phase transitions and thermal stability of the materials. TG provides information in two forms: mass change as a function of either temperature or time which is a direct indication and the derivative of mass loss (DTG) as a function of temperature or time which helps to pinpoint any shoulders present in data.³⁴ The micro-structural features of synthesized TaC powders were analyzed with field-emission scanning electron microscope (FE-SEM) (QUANTA 200 FEG) operating at 20 kV and transmission electron microscope (TEM) (JEOL 2100F) operating at 200 kV. The N₂ sorption studies for surface analysis were conducted using a BELSORP-max (BEL, Japan) to determine the Brunauer–Emmett–Teller (BET) surface area, the pore size, and the pore volume.

3. Results and discussion

3.1 Thermal Analysis of Ta-Ethoxide. The thermal stability and oxidation behavior of the Ta-E was analyzed by simultaneous DTA/TG in air. Fig. 1 gives the DTA-TG-DTG curves obtained for Ta-E. Initial mass loss in TG is due to loss of water. The exothermic DTA peak at 305 °C with corresponding mass loss in TGA curve is attributed to decomposition of Ta-E with evolution of CO₂ and H₂O (Equation 13). The exothermic DTA peak at 765 °C corresponds to formation of crystalline Ta₂O₅.³⁵ Formation of crystalline powder above 765 °C was used to determine the soaking temperature of 800 °C for the present work.

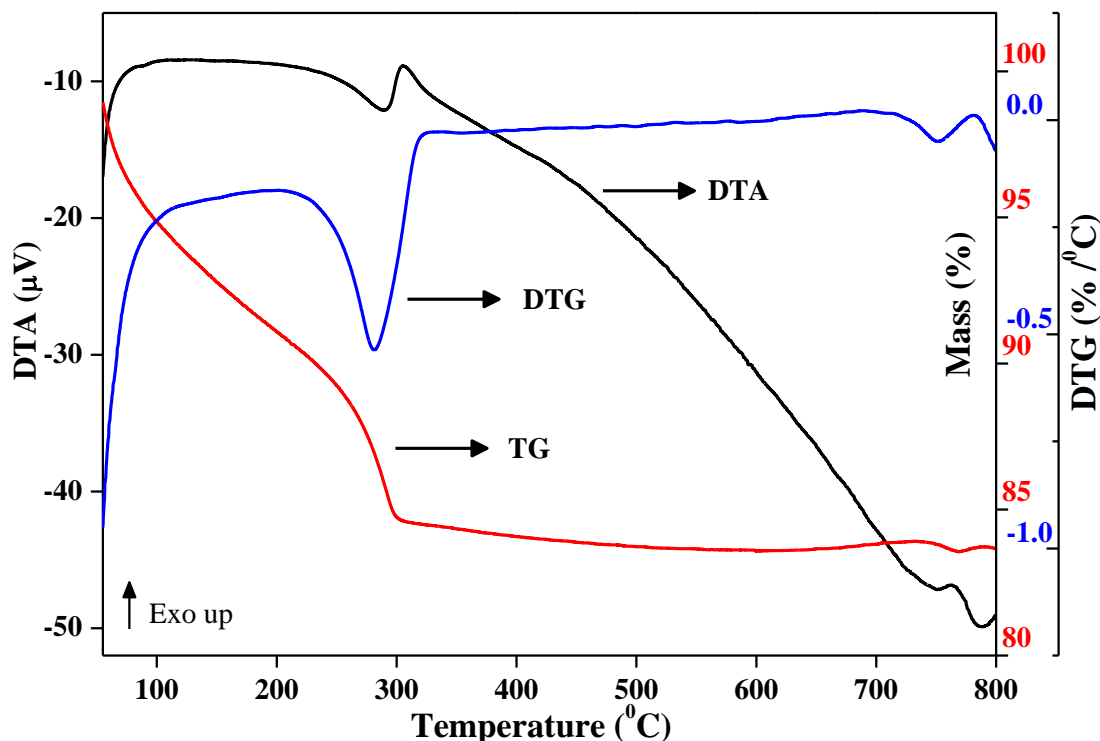
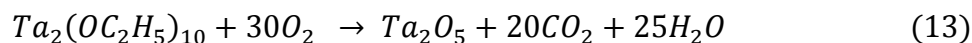


Fig. 1 DTA-TG-DTG of Ta-Ethoxide in air showing different transition points.

3.2 X-ray diffraction analysis (XRD) of the synthesized powders. Fig. 2 shows the XRD data of the synthesized samples after acid leaching. The XRD patterns of the as synthesized product for all the samples shows the presence of cubic TaC (ICDD Pattern – 01-089-2870) as dominant phase indicating that the formation of TaC has taken place during the reaction process. The minor phases have been identified as Ta₄O (ICDD Pattern – 00-015-0243) and hexagonal Ta₂C (ICDD Pattern – 00-032-1280). All the synthesized samples also contain hexagonal carbon (ICDD Pattern – 00-026-1076). As the soaking time is increased the concentration of the minor phases present as well as the peak locations and widths are changing. Table 1 gives details of the minor phases present for all the samples.

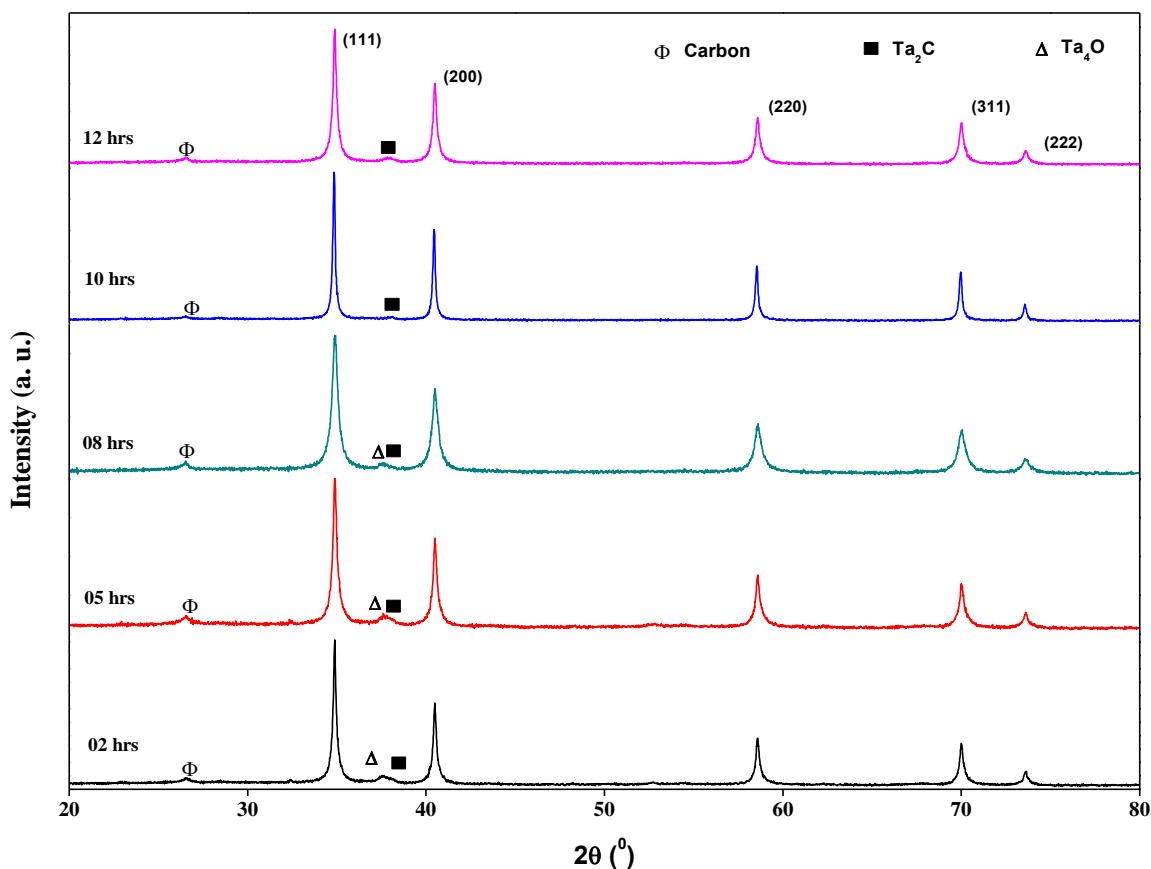


Fig. 2 XRD results of acid leached samples synthesized from Ta-E precursor with different soaking times at 800°C. TaC (peaks indexed) is the major phase formed for all the samples.

Table 1 The Minority phase(s), reliability factors for Rietveld refinement, lattice parameters and calculated carbon concentration in TaC_x phase of the synthesized samples.

Sample Name	Soaking Time	Minor Phases	χ^2	R_{wp}	a (nm)	x
2h	2 hrs	Ta ₄ O, Ta ₂ C	2.10	8.47	0.445547	0.990
5h	5 hrs	Ta ₄ O, Ta ₂ C	2.38	9.16	0.445557	0.991
8h	8 hrs	Ta ₄ O, Ta ₂ C	2.14	8.56	0.445533	0.989
10h	10 hrs	Ta ₂ C	1.99	7.57	0.445738	1.000
12h	12 hrs	Ta ₂ C	1.72	8.24	0.445532	0.985

Detailed analysis of the XRD patterns reveals that nearly 90% conversion to TaC has taken place even for 2h sample. However, the complete conversion to TaC needs 10 hrs. For the 10h sample

the minority phase T_4O is absent indicating complete reduction of the oxide and intensity of Ta_2C is also smallest for this sample. A further increase in soaking time results in an increase in the Ta_2C peak indicating that the carbon is getting removed from the TaC and the concentration of Ta_2C phase is increasing. The XRD data is best fitted with cubic space group $Fm-3m$ and it was observed that the lattice parameter changes as the synthesis time is varied. Fig. 3(a) gives the Rietveld refinement plots for the 10h sample.

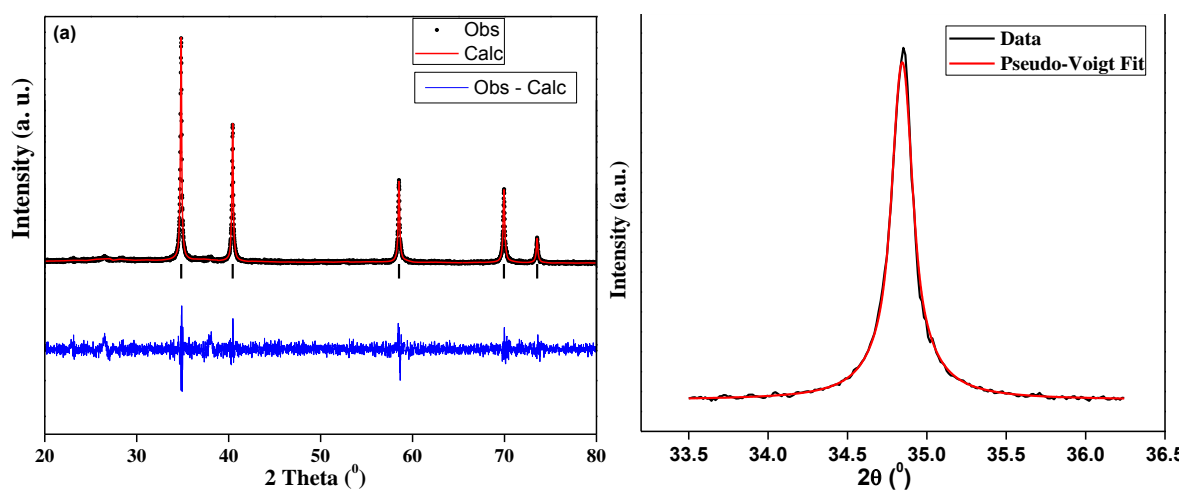


Fig. 3 (a) Rietveld refinement plots for the 10h sample. Measured data are indicated by dots and calculated data by solid curve. The difference between the measured and calculated data is given below as a plot, and tick marks indicate allowed peak positions. (b) The result of the pseudo-Voigt curve fit routine for the (111) peak of 10h sample.

The Wyckoff positions used for Rietveld refinement of XRD data are 4a (0,0,0) for Ta and 4b (0.5, 0.5, 0.5) for C. Table 1 gives the lattice parameters, R_{WP} and χ^2 – values obtained from the Rietveld refinement of the XRD data. The lattice parameter of the synthesized samples from the Rietveld refinement have been used to determine x , the fraction of C in the TaC_x .²⁵

$$a (\text{\AA}) = 4.3007 + 0.1563 x \quad (14)$$

The data (Table 1) clearly shows that for the 10h sample, the phase formed is $\text{TaC}_{1.0}$ (ICDD – 01-089-2870). With further increase in the soaking time the decrease in lattice constant supports the conjecture about the carbon loss from TaC as the soaking time is increased beyond 10 hrs.

Single line and double-Voigt integral breadth analysis methods have been used to determine the strain and size of the synthesized samples from the XRD profiles. Peak position (2θ), gaussian integral breadth (β_G) and lorentzian integral breadth (β_L) of the Bragg peaks from the XRD data were determined by profile fitting technique using pseudo-Voigt function. Fig. 3(b) shows the results obtained from the fitting of pseudo-Voigt function for the (111) peak for the 10h sample. Fig. 4 gives the single line and double-Voigt integral breadth method analysis graphs for the 10h sample. Similar graphs have been used to analyse all the samples. Table 2 gives the details of the size and strain values obtained for the single line and double-Voigt integral breadth methods. A comparison of the volume weighted particle sizes and strains obtained from single line method and the double-Voigt method shows that the single line method which takes into consideration only the Lorentzian contributions to size and Gaussian contributions to strain ends up overestimating the size and underestimating the strain in the samples.

From the single line analysis the strain obtained for the 8h sample is minimum and the size is comparable to 5h sample. This is counterintuitive since the peaks for 8h sample are broadest (Figure 2). Double-Voigt analysis shows that though the volume weighted column lengths for 2h, 5h and 8h samples are comparable but the surface weighted column length is actually smallest for 8h sample (Fig. 5(a)). This implies that the particle size and hence the surface area will be largest for 8h sample.

The analysis of XRD data (Table 1, 2) clearly shows that for the 10h sample the unit cell size, particle size and strain are maximum. Since double-Voigt method allows for the determination of

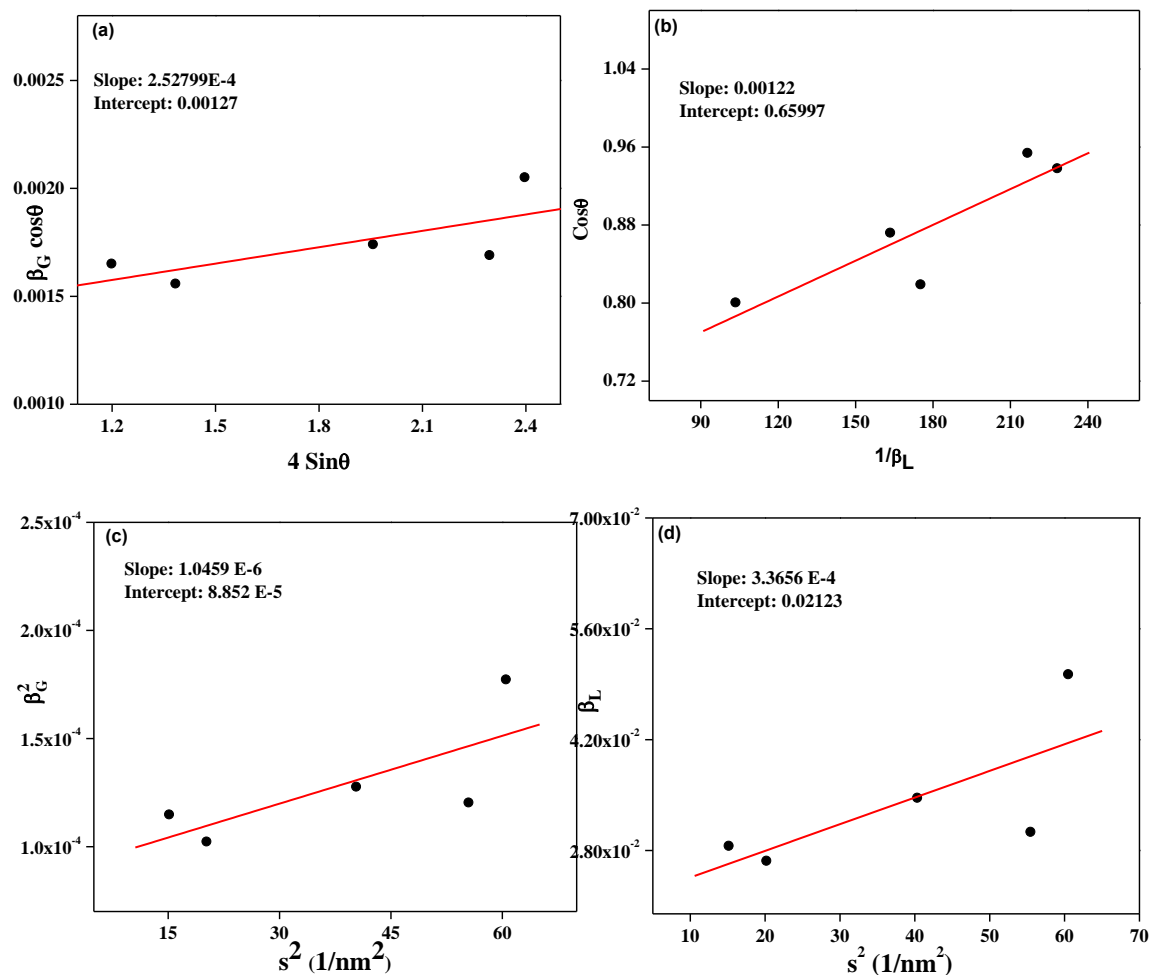


Fig. 4 Single line integral breadth analysis graphs of 10h sample. a) determination of maximum strain and b) determination of particle size. Double-Voigt Integral breadth analysis graphs ((c) and (d)) of 10h sample.

the r.m.s. strain distribution *w.r.t.* size and direction so the strains for different planes within the particles for synthesized samples are compared. For the 2h, 5h, 8h and 12h samples the r.m.s. strains are isotropic. Inset in Fig. 5(b) shows the variation of the strain in all the directions for 8h sample. But for the 10h sample the strain for the (111) plane is very large (Fig. 5(b)) as compared to that for the other planes. The large amount of strain present in (111) plane may be due to complete filling of octahedral voids with carbon for this sample. The same may also be responsible for increasing the unit cell size and the particle size.

The results of XRD data analysis show that both 8h and 10h samples are good prospective candidates for the electro-catalytic activities; the 10h sample due to its enhanced strain which makes it more reactive and the 8h sample due to its larger surface area which provides more reaction sites. The electrochemical activity of both the samples will need to be probed to assess the comparative importance of strain and surface area for the catalytic activities.

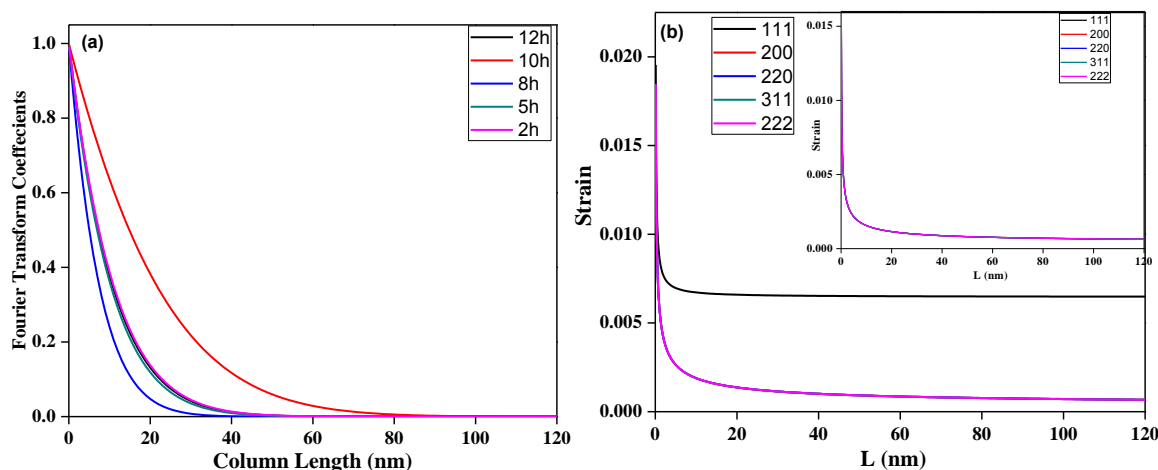


Fig. 5 (a) Fourier transform coefficients as a function of column length (L) for all the synthesized samples. The initial slope of this graph is used to determine the surface weighted particle size. (b) Strain as function of column length (L) for all the indexed planes for the 10h sample. Inset shows isotropic nature of the strain in 8h sample.

Table 2 Structural data for synthesized samples as determined from the single line and double-voigt integral breadth methods from XRD profile analysis.

Sample Name	Single-Line Analysis			Double-Voigt Analysis	
	Crystallite size (nm)	Max Strain ($\times 10^{-4}$)	r.m.s. Strain ($\times 10^{-4}$)	$\langle D_v \rangle$ (nm)	$\langle D_s \rangle$ (nm)
2h	71	2.14	1.71	22	13
5h	39	2.37	1.89	20	12
8h	39	0.71	0.56	21	8
10h	113	2.53	2.02	45	25
12h	49	2.30	1.83	21	12

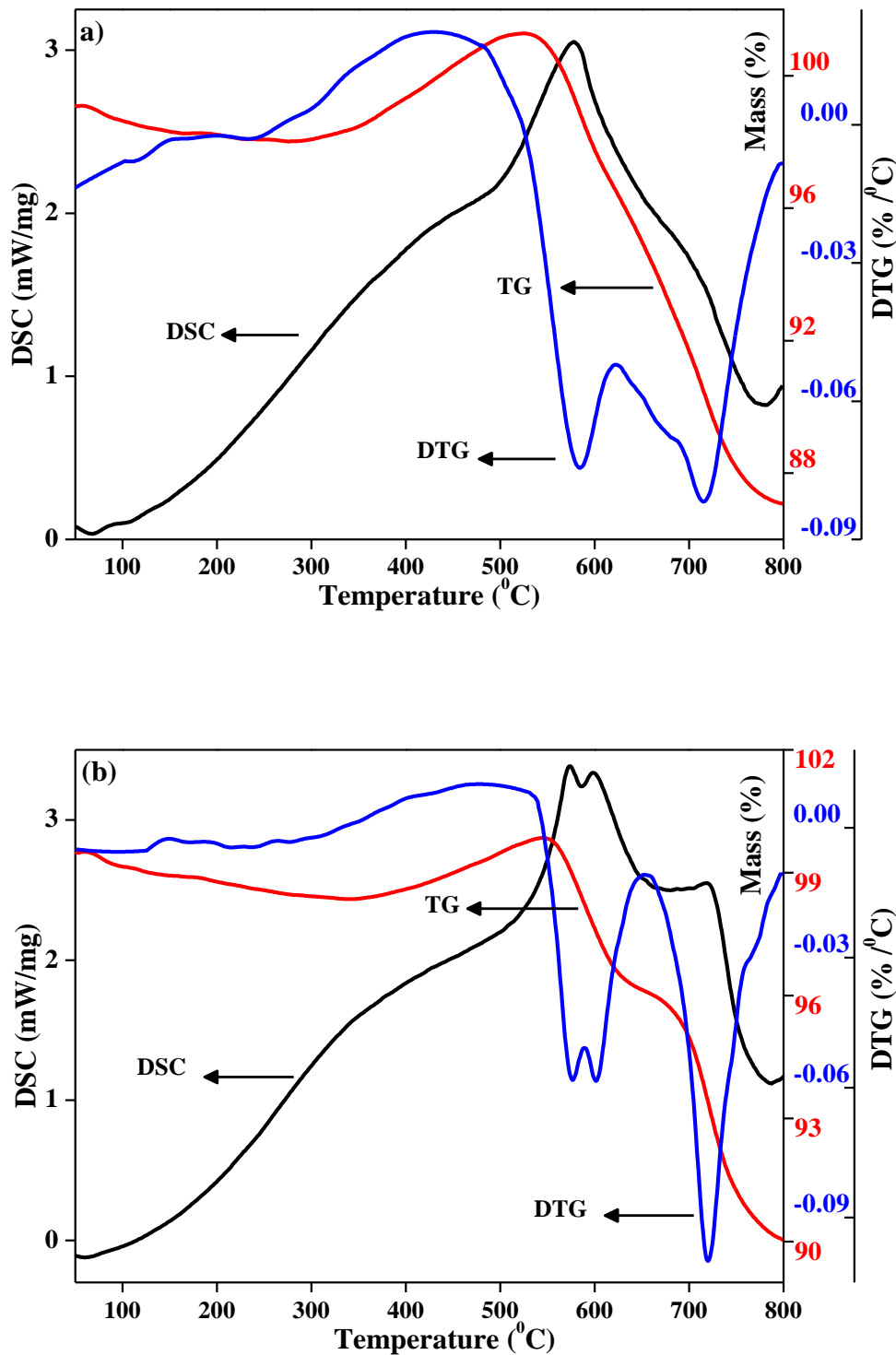


Fig. 6 DSC-TG-DTG curves of sample (a) 2h (b) 10h. For the 10h sample the peaks for carbon removal and oxidation are well separated.

3.3 Thermal Analysis of synthesized powders. The thermal stability and oxidation resistance of the obtained powders was analyzed by DSC/TG. Fig. 6 (a) shows the DSC-TG-DTG curves for 2h sample and this data is representative for all the synthesized samples except the 10h sample where the decarburization and oxidation events are distinct from each other (Fig. 6 (b)). The data obtained from analysis of the DSC-TG-DTG curves is given in Table 3.

Initial heating from room temperature onwards results in mass loss which is followed by mass gain. The initial mass loss is indicative of the amount of chemical species adsorbed onto the surface of the particles.²² For our samples before oxidation nearly 2 mass% of surface adsorbed species is removed. This corresponds to potentially large surface area available for adsorption. The start of mass gain in TG curve is an indicator of the stability of the synthesized samples since the weight gain in the samples is due to oxidation of TaC resulting in formation of Ta₂O₅ and CO₂.⁸ The 2h and 5h samples have nearly the same oxidation stability (Table 4) but as the soaking time is increased the samples are becoming more stable. The 10h sample is most stable for oxidation in air with the weight gain in TG starting at around 339 °C (Fig. 6 b)). The 12h sample shows decrease in stability which is expected as it is carbon deficient.

The first peak in DTG with a corresponding exothermic peak in DSC and maximum mass gain in TG gives the temperature for the conversion of TaC into Ta₂O₅. This conversion is a two-step process: release of carbon from the TaC followed by oxidation. For the TaC_x (x<1) samples the two processes occur simultaneously as there are already carbon vacancies present in the system. But for the case where x = 1 (10h sample) the oxidation occurs after the removal of carbon and the DSC as well as DTG curve show well defined peaks for the two processes: the carbon removal occurring at 573 °C followed by oxidation at 598 °C (Fig. 6(b)). The ΔH values

represent the amount of heat required for a reaction and were determined from the total area enclosed by the thermal analysis peak using software package provided with the thermal analyzer. The ΔH for the two processes is 25.73 J/g and 21.2 J/g respectively. The high temperature peak (>700 °C) in DTG curve, with a corresponding peak/hump in DSC, occurs at nearly the same temperature for all the samples and is attributed to oxidation and combustion of the carbonaceous residue.¹³

Table 3 The data obtained from the analysis of the DSC-TGA-DTG curves and BET analysis of the synthesized samples.

Sample Name	Weight gain start (°C)	DSC main peak (°C)	DTG peak 1 (°C)	DTG peak 2 (°C)	Average Pore diameter (nm)	Surface Area (m ² /g)	Pore Volume (cm ³ /g)
2h	167	578	584	715	12.244	74.909	0.2293
5h	162	595	604	710	12.404	95.383	0.2958
8h	183	586	590.5	716	9.1541	159.67	0.3654
10h	339	573 598	576 601	720	14.023	44.851	0.1572
12h	206	580.4	581	721	14.199	56.113	0.1992

If the sample consists of pure TaC, its oxidation will result in 14.5% increase in mass. In our case this is never achieved. Maximum increase encountered is nearly 4.5 mass% after the initial weight loss stops for the 8h sample. This small increase in mass as compared with the expected value is due to the presence of carbonaceous content in the synthesized samples.⁸ The presence of carbonaceous residue is indicated/supported by XRD data as well as TEM images. As the sample is heated the mass increase due to oxidation is being offset by the decrease in mass due to oxidation of carbonaceous residue. The residual mass at 800 °C for all the samples is 85-90%. This leads to the conclusion that the carbonaceous content in our samples ranges from 20-25 %.³⁶ All the TGA curves become nearly stable after 780 - 795 °C. Even heating up to 1200 °C further

shows a loss of 1% indicating that carbonaceous substance is not removed completely (data not shown). So the determination of exact TaC content in the individual samples is not possible.

3.3 Microstructure analysis. Fig. 7 shows the representative FE-SEM image of the final product synthesized for 10h sample. It is clear from the images that particles have a tendency to agglomerate and the size distribution is inhomogeneous. The analysis of the morphology of particles in FE-SEM images shows that most of the powders are faceted and their size varies from 60-100 nm.

Fig. 8(a-b) shows the representative TEM images of the synthesized TaC nanoparticles for 10h sample. The presence of carbon coating on the surface of each particle is clearly visible. Moreover, the morphology of carbon coated nanoparticles varies from faceted to spherical and they have a tendency to aggregate. Fig. 8(c) gives the High Resolution-TEM (HRTEM) image of a single crystalline TaC nanoparticle and shows the (111) facets of the particle. The distance between the adjacent lattice fringes is the interplanar distance of cubic TaC (111), which is 0.26 nm (ICDD Pattern – 01-089-2870). This suggests that the synthesized TaC powder has cubic crystalline structure.

It is observed from TEM images that the particle size distribution is broad (Fig. 8(d)). The particle size measurement was done on nearly 100 particles from different areas/scans and follows the well documented log-normal distribution.³⁷ The log-normal probability distribution (Fig. 8(d)) is calculated by adopting the following equations:

$$f(d) = \frac{1}{\sqrt{2\pi} d \log \sigma_g} \exp \left\{ -\frac{(\log d - \log \mu_g)^2}{2(\log \sigma_g)^2} \right\} \quad (15)$$

$$\log \sigma_g = \sqrt{\frac{\sum(\log d_i - \log \mu_g)^2}{\sum n_i}} \quad (16)$$

$$\log \mu_g = \frac{\sum \log d_i}{\sum n_i} \quad (17)$$

Where $f(d)$ denotes the log-normal distribution, d the particle diameter, n_i the number of particles with diameter d_i , $\log \mu_g$ the mean diameter and σ_g is the geometrical standard deviation, respectively. The average size of the prepared TaC nanoparticles is in the range of 20 to 40 nm for the reaction time of 10 hrs. The size obtained from the TEM is comparable to that obtained from the double-Voigt integral breadth analysis.

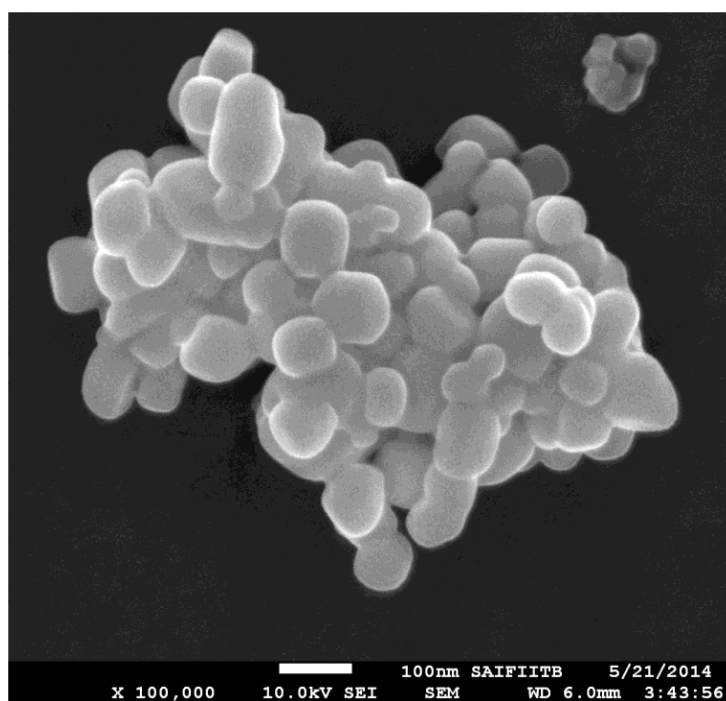


Fig. 7 FE-SEM micrograph of TaC nanopowder for 10h sample showing faceted to spherical morphology.

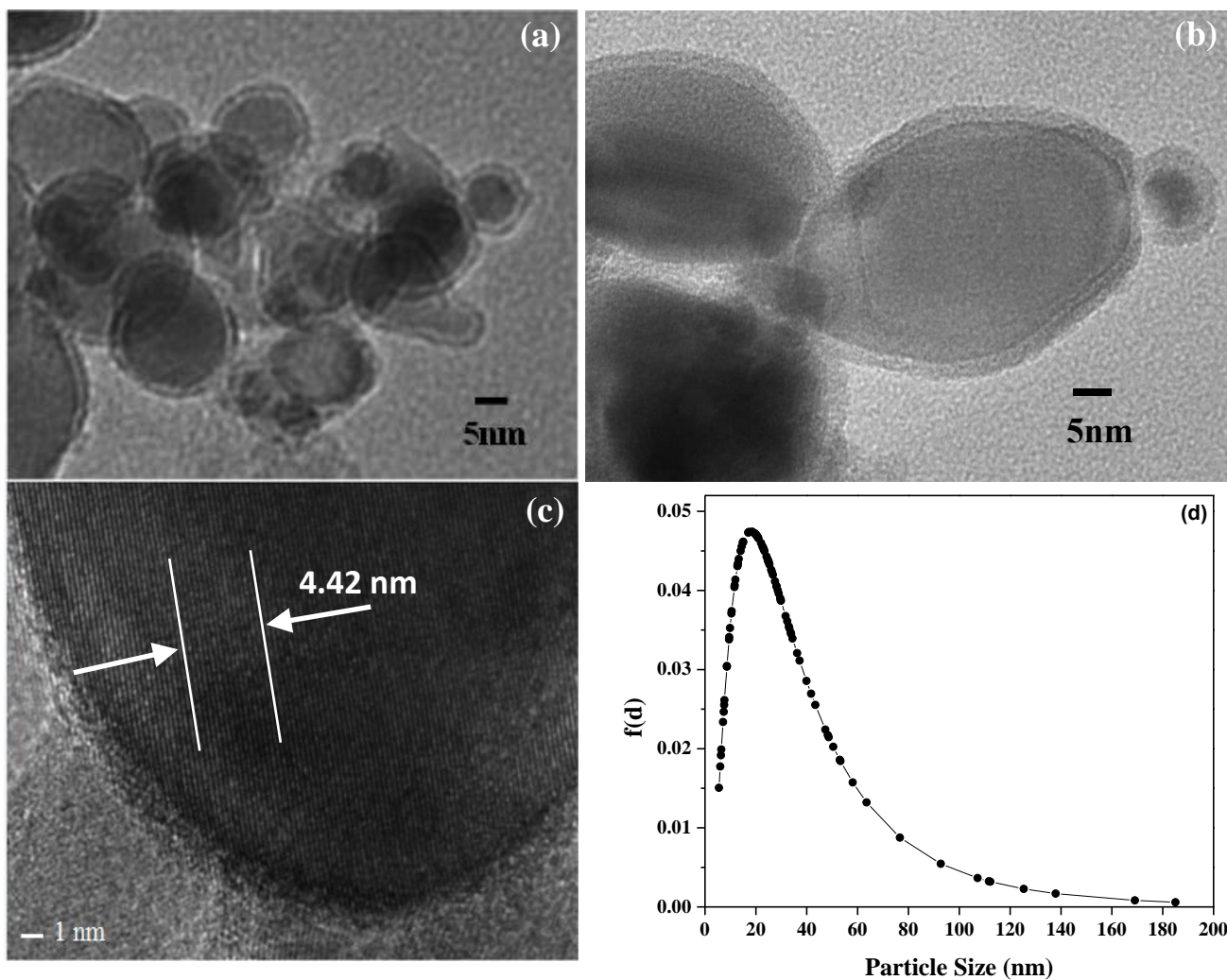


Fig. 8 (a-b) TEM micrographs of TaC nanopowder for the 10h sample. The agglomerated particles have nearly spherical morphology and are evenly coated with a carbon layer. (c) HRTEM micrograph of TaC nanopowder for 10h sample showing lattice fringing. (d) Particle size distribution for 10h sample from TEM.

3.4 BET Surface area analysis: N₂ sorption studies were done to obtain the BET surface area of the synthesized samples. The results are listed in Table 3. The data shows that initially the surface area of the product increased with the increasing soaking time with maximum area of 159.67 m²/g obtained for the 8h sample. A further increase in time results in decrease in the surface area. This is most likely due to increase in particle size for the 10h sample as is evident from the XRD analysis.

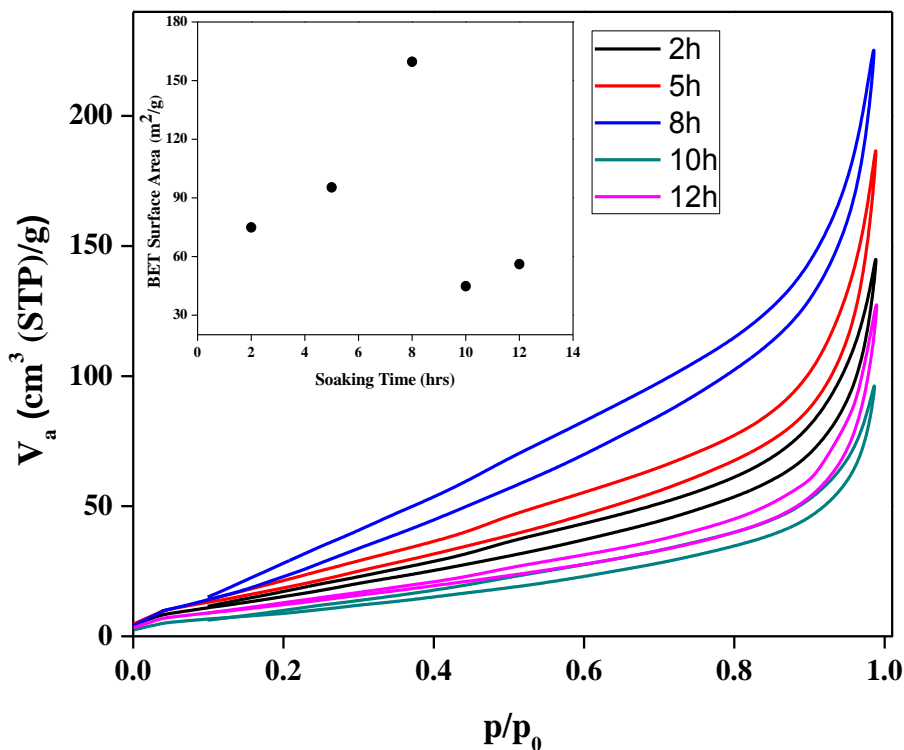


Fig. 9 N₂ adsorption-desorption isotherms for the synthesized samples. Inset shows the variation of BET surface area for the synthesized samples with increasing soaking time.

Fig. 9 shows the N₂ adsorption-desorption isotherms for the synthesized samples. The adsorption isotherms exhibit the characteristics of a type-II isotherm according to IUPAC classification.^{3,38}

An empirical classification of the hysteresis loops which gives information about the texture of the adsorbent has also been given by IUPAC and the isotherms show H-4 hysteresis

characteristics.^{38,39} This implies that the powders are forming a complex structure with both micropores and mesopores. This behaviour is because of agglomeration of particles in the synthesized product.

3.5 Proposed mechanism for TaC formation: During heating of the autoclave, Mg being highly reactive substance absorbs oxygen from the air present inside the autoclave and forms MgO. In conjunction with low temperature heating experiments (500 °C, 2 hrs, Fig. 10) and earlier reported data about decomposition of Ta-E,²³ the Ta-E decomposes initially into tetrahedral TaO (ICDD card no – 00-17-0709).

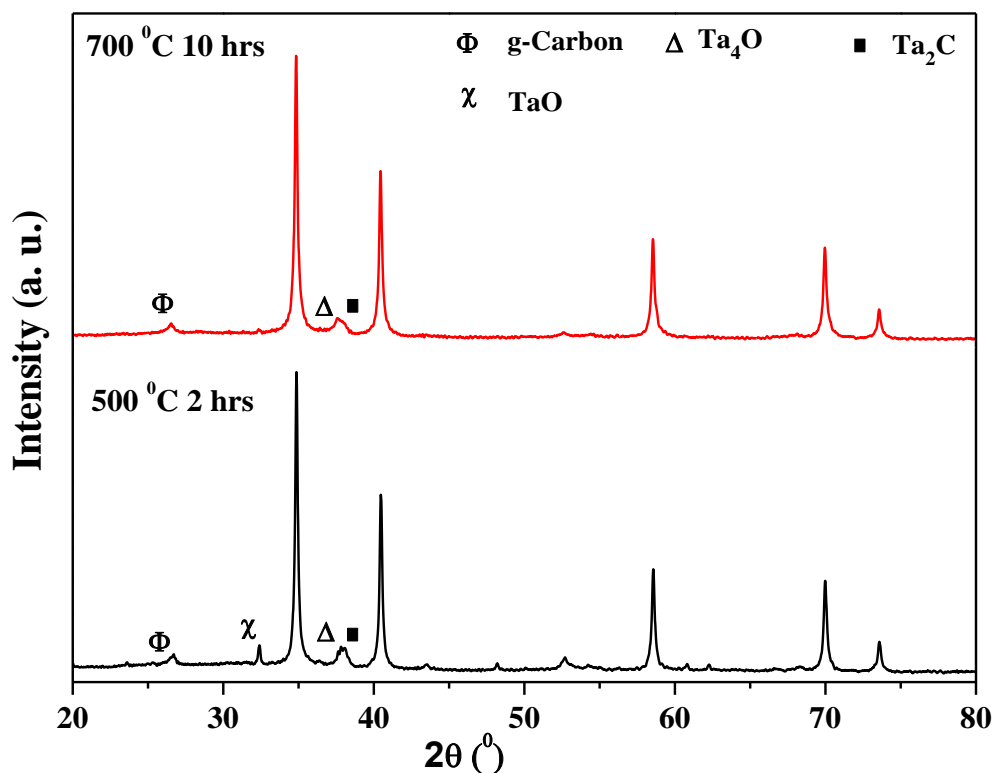


Fig. 10 XRD data for 700 °C 10hrs and 500 °C 2hrs samples.

The exact nature of the gaseous organic intermediate(s) cannot be determined as the decomposition of Ta-E is taking place in a closed oxygen deficient environment. MgO is one of the most active catalysts for reduction.⁴⁰ Hence, its presence results in reduction of the gaseous organic compounds to hydrogen and carbon.

Since the carbon is present in excess in Ta-E so the amount of carbon produced is high enough to completely coat the initially formed TaO powder. This carbon coating helps to increase the reaction rate for reduction and carburization by ensuring the close proximity of the reactants. Moreover, the carbon coating also prevents the oxide particles from coalescing which ensures that the final product is in nanometer range.³⁵ The initially formed TaO transforms to TaC via formation of Ta₄O and Ta₂C (Fig. 2). In the entire set of experiments no evidence of Ta was found in any of the samples, rather Ta₂C was present. Since the carbon is present in sufficiently high concentration so it is possible that Ta obtained from reduced oxide may get converted into Ta₂C immediately and then to TaC. Fig. 11 gives the schematic of the proposed mechanism. In the present system the formation of TaC starts with the reduction of TaO rather than Ta₂O₅ so this leads to lowering of reaction/formation temperature and time.

Reaction rate within the autoclave is also very high as is evident from the nearly 80-90 % conversion within 2 hrs for all the temperatures (data not shown). However, the complete conversion needs 10 hrs at 800 °C (Fig. 2 and 10). The higher time required for complete conversion is because of the fact that in the initial stage diffusion of carbon through the surface leads to formation of TaC on the outer surface of the particle and this formed TaC layer creates hindrance for further diffusion of carbon inside. The large concentration of carbon in the outer coating still facilitates the diffusion of carbon into inner unreacted core even through the TaC.

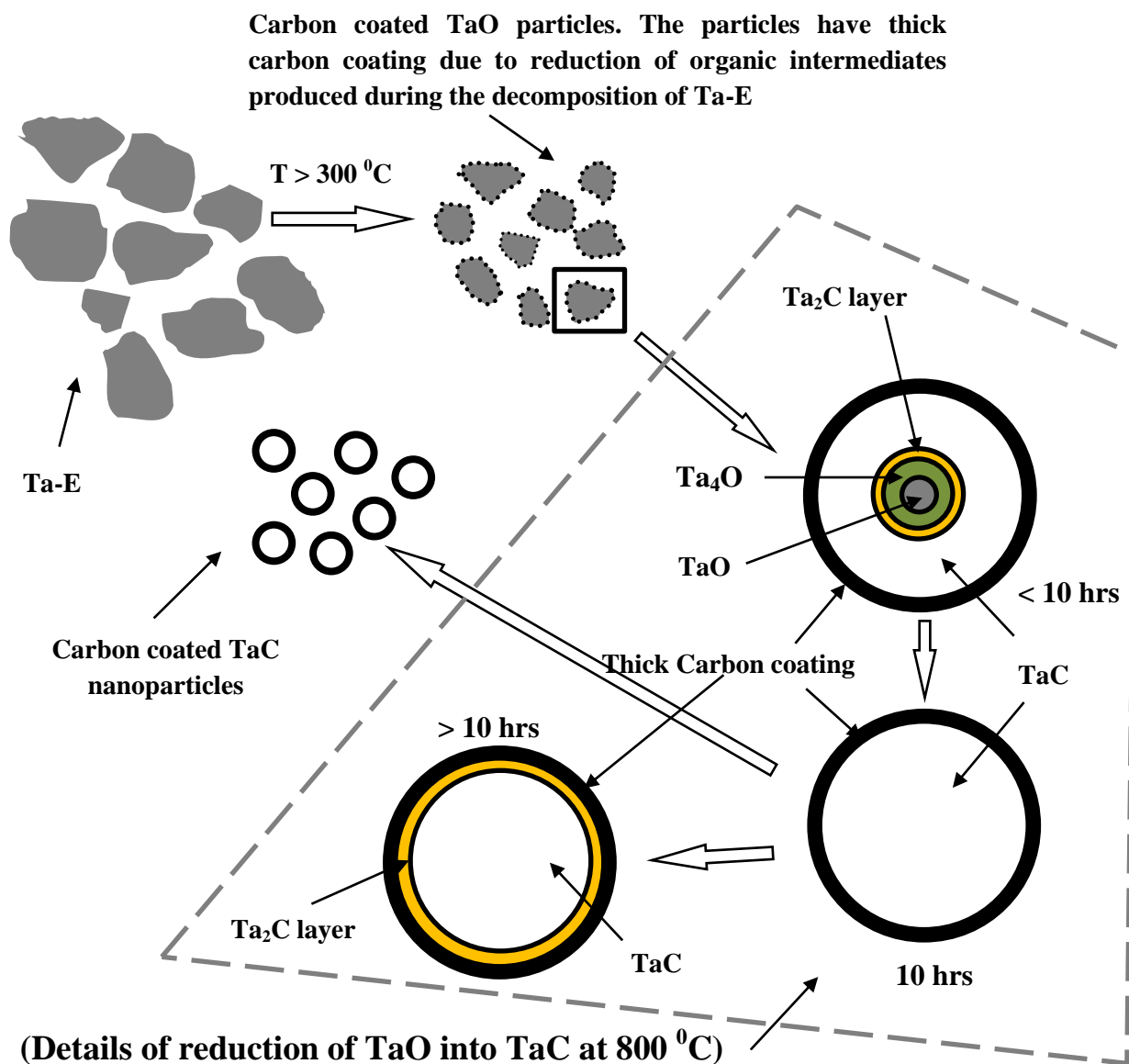


Fig. 11 The proposed mechanism for transformation of Ta-E into carbon coated TaC nanoparticles.

However, the carbon atoms now need to travel longer distance which makes the final process time dependent as the diffusion path of carbon increases with time as the reaction progresses. In order to facilitate the entire process the travel rate of carbon can be made faster by increasing the holding temperature as is evident from Fig. 10 where complete conversion is not taking place at 700 °C in the same time duration (10 hrs) as has been obtained at 800 °C (Fig. 2).

4. Conclusions

High surface area carbon-coated TaC nanosized powder has been synthesized successfully in single step by the chemical reaction method using Ta-E as the precursor as well as carbon source. The maximum carbon content (TaC_x , $x=1$) with complete oxide removal is obtained for 10 hr samples. XRD analysis shows that the 10 hr samples have the largest unit cell size as well as the highest strain concentrated in (111) plane. This may be due to completely filled octahedral voids. Thermal stability analysis in air for the 10h sample shows that among the synthesized samples it is most stable with well separated carbon removal and oxidation events. All the other samples show isotropic strain. Thermal analysis, XRD and microstructure analysis results have been used to predict the mechanism for the formation of the carbon coated nano-TaC particles.

The presence of graphitic carbon along with the nano-size of the powders makes the final product a good candidate for superior consolidation properties.^{41,42} Samples obtained from the present method have high surface area and are also strained. Both these conditions are conducive for high absorption of the reactant species and hence make the synthesized powders good candidates for catalytic applications. Presence of adherent carbon coating on the surface is favorable for the material so as to have conductive behavior of both C and TaC. The carbon

coating will also contribute towards the stability of the powders in the harsh environments in reaction chambers.

Acknowledgements

The authors are grateful to SAIF, IIT Bombay for providing FE-SEM, SAI Labs, Thapar University for providing XRD and AIRF, JNU, Delhi for providing TEM. One of the authors (O. P. Pandey) is thankful to Department of Science and Technology (DST), New Delhi, India to which a grant proposal has been submitted.

References

1. M. Ali, M. Ürgen, M. A. Atta, A. Kawashima and M. Nishijima. *Mater. Chem. Phys.*, 2013, **138**, 944-950.
2. C. L. Yeh and E.W. Liu, *J. Alloys Compd.*, 2006, **415**, 66–72.
3. Y.-J. Lee, S. H. Kima, T.-H. Lee, H. H. Nersisyanb, K.-H. Lee, M.-H. Hana, S.-U. Jeong, K.-S. Kang, K.-K. Bae and J.-H. Lee, *Chem. Eng. Sci.*, 2014, **107**, 227–234.
4. Choi J-G. *J. Porous. Mater.*, 2013, **20**, 1059–1068.
5. L. Silvestroni, A. Bellosi, C. Melandri, D. Sciti, J. X. Liu and G. J. Zhang, *J. Eur. Ceram. Soc.*, 2011, **31**, 619–627.
6. J. P. Kelly, R. Kanakala and O. A. Graeve, *J. Am. Ceram. Soc.*, 2010, **93**, 3035–3038.
7. J. Ma, Y. Du, M. Wu and M. C. Pan, *Mater. Lett.* 2007, **61**, 3658–3661.
8. N. S. Alhajri, H. Yoshida, D. H. Anjum, A. T. Garcia-Esparza, J. Kubota, K. Domend and K. Takanabe, *J. Mater. Chem. A* 2013, **1**, 12606-12616.

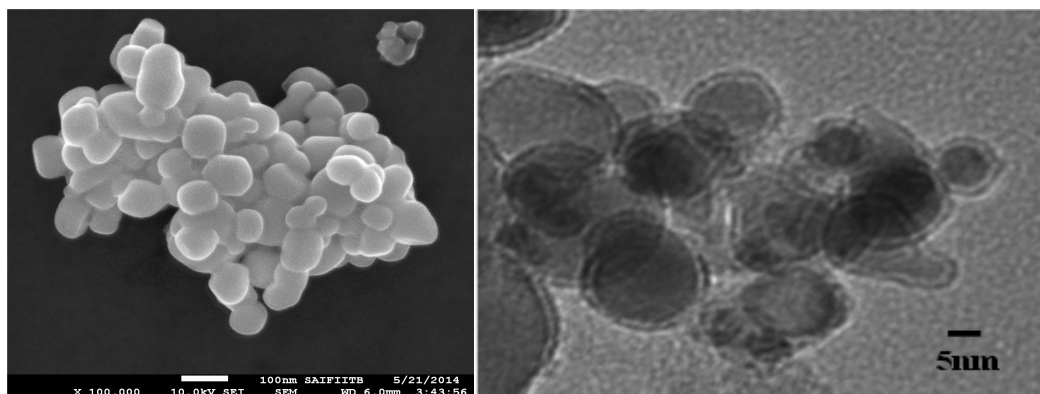
9. J. Polonsky', I. M. Petrushina, E. Christensen, K. Bouzek, C. B. Prag, J. E. T. Andersen and N. J. Bjerrum, *Int. J. Hydrogen Energy*, 2012, **37**, 2173-2181.
10. A. L. Stottlemyera, T. G. Kellya, Q. Meng and J. G. Chen, *Surf. Sci. Rep.*, 2012, **67**, 201–232.
11. D. J. Ham and J. S. Lee, *Energies*, 2009, **2**, 873-899.
12. A. Ishihara, M. Tamura, Y. Ohgi, M. Matsumoto, K. Matsuzawa, S. Mitsushima, H. Imai and K. Ota, *J. Phys. Chem. C*, 2013, **117**, 18837–18844.
13. D.-H. Kwon, S.-H. Hong and B.-K. Kim, *Mater. Chem. Phys.*, 2005, **93**, 1–5.
14. M. Ma, W. Shen, P. Zhang, J. Zhang, Q. Wang and C. Ge. *Mater. Lett.*, 2011, **65**, 96–99.
15. V. G. Sevast'yanov, E. P. Simonenko, N. .A Ignatov, Y. S. Ezhov and N. T. Kuznetsov. *Inorg. Mater.*, 2010, **46**, 495–500.
16. H. I. Won, N. Hayk, C. W. Won and H. H. Lee *J. Mater. Sci.*, 2011, **46**, 6000–6006.
17. P.G. Li, M. Lei and W. H. Tang, *Mater. Res. Bull.*, 2008, **43**, 3621–3626.
18. P. G. Li, M. Lei, Z. B. Sun, L. Z. Cao, Y. F. Guo, X. Guo and W. H. Tang, *J. Alloys Compd.*, 2007, **430**, 237–240.
19. A. M. Nartowski, I. P. Parkin, M. Mackenzie and A. J. Craven, *J. Mater. Chem.*, 2001, **11**, 3116–3119.
20. Y.-J. Chen, J.-B. Li, Q.-M. Wei and H.-Z. Zhai, *Mater. Lett.*, 2002, **56**, 279– 283.
21. H. Xiang, Y. Xu, L. Zhang and L. Cheng, *Scripta. Mater.*, 2006, **55**, 339–342.
22. J. P. Kelly and O. A. Graeve, *J. Am. Ceram. Soc.*, 2011, **94**, 1706–1715.
23. H. He, K. Zhou, X. Xiong and B. Huang, *Mater. Lett.*, 2006, **60**, 3409–3412.
24. H. He, K. Zhou and X. Xiong, *J. Mater. Sci. Technol.* 2005, **21**, 381-385.
25. A. L. Bowman, *J. Phys. Chem.*, 1961, **65**, 1596-1598.

26. Y. Yosida and I. Oguro, *Physica C*, 2006, **434**, 138–140.
27. A. Kumar, K. Singh and O. P. Pandey, *Physica E*, 2009, **41**, 677–84.
28. G. Singla, K. Singh and O. P. Pandey, *Ceram. Int.*, 2014, **40**, 5157–64.
29. S. Vives, E. Gaffet, and C. Meunier, *Mater. Sci. and Eng. A*, 2004, **366**, 229–38.
30. G. Singla, K. Singh and O. P. Pandey, *Appl. Phys. A*, 2013, **113**, 237–42.
31. D. Balazar, In: R. L. Snyder, J. Fiala and H. J. Bunge, editors, *Defect and Microstructure Analysis by Diffraction*, Oxford, U.K.: Oxford University Press; 1999. p. 94–126.
32. K. Santra, P. Chatterjee and S. P. S. Gupta, *Bull. Mater. Sci.*, 2002, **25**, 251–57.
33. Merkus HG. *Particle Size Measurements: Fundamentals, Practice, Quality*. Dordrecht, Netherland: Springer Science & Business Media B.V; 2009. p. 1–42.
34. R. Díaz-Ayala, L. Arroyo-Ramírez, R. G. Raptis and C. R. Cabrera, *J. Therm. Anal. Calorim.*, 2014, **115**, 479–88.
35. H.-C. Huang and T.-E.Hsieh, *J. Appl. Polym. Sci.*, 2010, **117**, 1252–59.
36. A. L. Tomas-Garcia, Q. Li, J. O. Jensen, N. J. Bjerrum, *Int. J. Electrochem. Sci.*, 2014, **9**, 1016–1032.
37. B. Debalina, M. Kamaraj, S. R. Chakravarthi, N. J. Vasa, and R. Sarathi, *Plasma Sci. Technol.*, 2013;**15**, 562–69.
38. W. Wang, P. Liu, M. Zhang, J. Hu and F. Xing, *Open J. Compos. Mater.*, 2012, **2**, 104–12.
39. M. Thommes *Chem. Ing. Tech.*, 2010, **82**, 1059–73.
40. V. K. Díez, C. R. Apesteguía and J. I. Di Cosim, *Lat. Am. Appl. Res.*, 2003, **33**, 79–86.
41. A. Gubernat, *J. Eur. Ceram. Soc.*, 2013, **33**, 2391–2398.

42. D. Lahiri, E. Khaleghi, S. R. Bakshi, W. Li, E. A. Olevsky and A . Agarwal, *Scripta Mater.*, 2013, **68**, 285–88.

Table of contents entry

Colour graphic:



Novelty of the work:

Carbon-coated nano-TaC has been synthesized at 800⁰C using Tantalum-Ethoxide by single step chemical reaction route and no external carbon source